Eur. Phys. J. Special Topics **145**, 125–136 (2007)

DOI: 10.1140/epjst/e2007-00151-6

THE EUROPEAN PHYSICAL JOURNAL SPECIAL TOPICS

Nodal patterns of floaters in surface waves

S. Lukaschuk[1,a], P. Denissenko[1], and G. Falkovich[2]

[1] Fluid Dynamics Laboratory, The University of Hull, Hull HU6 7RX, UK
[2] Physics of Complex Systems, The Weizmann Institute of Science, Rehovot 76100, Israel

Abstract. We argue theoretically and demonstrate experimentally that in a standing wave floating particles drift towards the nodes or anti-nodes depending on their hydrophilic or hydrophobic properties. We explain this effect as the breakdown of Archimedes' law by a surface tension, which creates a difference between the masses of the floater and displaced liquid, making the particle effectively inertial. We describe analytically the motion of a small floating particle in a small-amplitude wave and show that the drift appears as a second order effect in wave amplitude. We confirm experimentally that indeed the clustering rate is proportional to the square of the wave amplitude. In the case of surface random waves we show experimentally that the inertial effects significantly change the statistics of floater distribution on a liquid surface. The analysis of particle concentration moments and probability distribution functions shows that particle concentrate on a multi-fractal set with caustics.

1 Introduction

How do small particles behave in an oscillating environment? Historically the first answer to this question was obtained in 1787 by the German physicist Chladni for particles on a solid surface, that oscillate in a standing wave. The Chladni figures consist of nodal lines which are formed by sprinkling fine sand on a vibrating surface which jumps away from the areas with large vibration amplitude and remains in the nodal areas where the amplitude is nearly zero. In this way, Chladni invented a technique to visualize mechanical vibration modes of a rigid plate. In some cases particles on the vibrating plate can gather in anti-nodes. In 1827 Savart [1] described an experiment where he observed that very fine powder, such as lycopodium, settles in the antinodes instead of nodes. As it was explained later by M. Faraday [2] this is due to the action of the air currents – lycopodium powder returns to the nodes in a vacuum.

The second case was discovered one hundred years after Chladni: in 1866 Kundt demonstrated visualization of a standing acoustic wave in a long tube whose interior walls were covered by fine light powder or dust. When the sound wave was excited in a gas filling the tube, the dust particles assembled into the heaps at the wave nodes. Besides the visualization of sound waves, the Kund effect also provided a possibility to measure the velocity of sound in gases. The nature of the Kundt effect is different from that of Chladni. In the Kundt case the particle movement is due a nonuniform acoustic radiation pressure in a standing wave [3]. The same force is responsible for the clustering of small particles by a standing ultrasound wave in a liquid suspension [4].

One may find it hard to believe that the third case (of nodal patterns created by particles on an oscillating liquid surface) was discovered more that hundred years after Kundt [5]. In a small-amplitude wave floaters do not jump so that the Chladni effect is absent. On the other hand, the pressure is uniform over the surface so that the Kundt effect is absent too. The

[a] e-mail: S.Lukaschuk@hull.ac.uk

absence of particle bouncing and the pressure gradient created a widespread perception that small particles just stick to a liquid surface and move with it. What is missing from this picture is the account of surface tension, which is important precisely for small particles. The surface tension changes a submersion depth and makes a particle lighter or heavier than the displaced liquid. That means that small floaters are inertial so that they can move relative to the fluid. Indeed, a small floater on a stationary inclined liquid surface (formed, say, near boundaries) drifts along the slope [7,8]. On an inclined surface of water, a hydrophobic particle (a small piece of plastic, pollen grain or even a drop of oil) slides down, while a hydrophilic particle (glass hollow sphere) climbs up. In a standing wave, particle inertia produces a well noticeable particle clustering correlated with a wave nodal pattern, see Fig. 1.

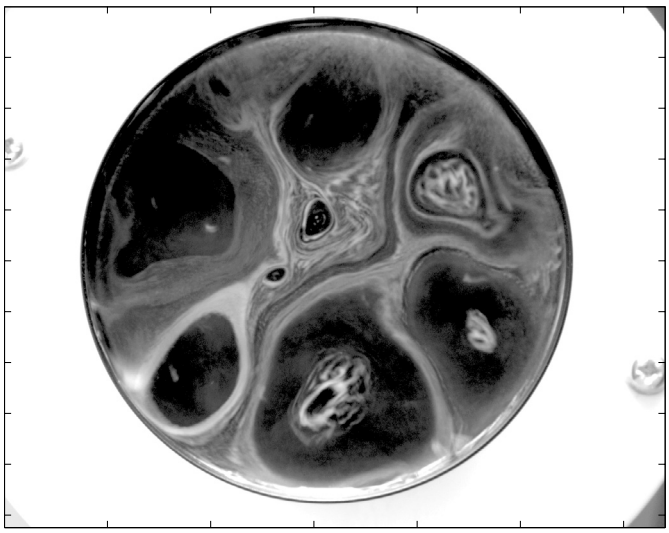

Fig. 1. Clustering of suspension of floating particles in capillary waves. The particles are 30 μm hollow glass spheres of density $0.6\,\mathrm{g/cm^3}$ deposited on a surface of a water filled Petri dish. The capillary waves are excited by vertical vibrations.

It should be noted that the deformation of the liquid surface caused by floaters and capillarity-induced drift along the slope cause the interaction between floaters. On a horizontal surface two identical floating spheres will attract each other with force proportional to their diameter in power six [9]. This interaction force is rather weak for small particles and their clustering can be easily destroyed by weak shear flow. An estimation shows that the attraction force between hollow glass spheres (density - $0.6\,\mathrm{g/cm^3}$, diameter 100 μm, contact angle - zero) is less than the Stokes drag generated by a shear flow with the velocity gradient $2 \cdot 10^{-5}\,\mathrm{s^{-1}}$.

To explain the drift of a single particle in a standing surface wave one needs to take into account two contributions to the net force averaged over the wave period. The first one is related to the fact that a particle placed between a node and antinode moves on a surface that is steeper nearer the node, see Fig. 2. In Figure 2 the lines A and B show the positions of the water surface separated by a half period. Dotted arrows show the corresponding displacements of the points on the fluid surface and the particles in between the node and loop. The particle motion is vertical at the antinode (maximum of elevation), horizontal at the node and inclined in between. One can see see that the lower position is closer to the node so that it corresponds to a steeper slope and then to a larger force. As a result there is a net force pushing a hydrophobic (heavier) particle towards the antinode and hydrophilic (lighter) particle towards the node. The second contribution is due to the vertical displacement of the inertial floater with respect to the surface. The oscillation of this displacement has the opposite signs for the "heavy" hydrophobic and "light" hydrophilic particles. Indeed, acceleration of the fluid surface is downwards/upwards at A and B respectively so that effective gravity is smaller at A than at B. Therefore, the hydrophilic particle at D_A is submerged deeper than at D_B and the hydrophobic one vise versa (compare C_A and C_B). This consideration presumes that the wave frequency is smaller than the resonant frequency of the particle free oscillations relative to the surface, which is always

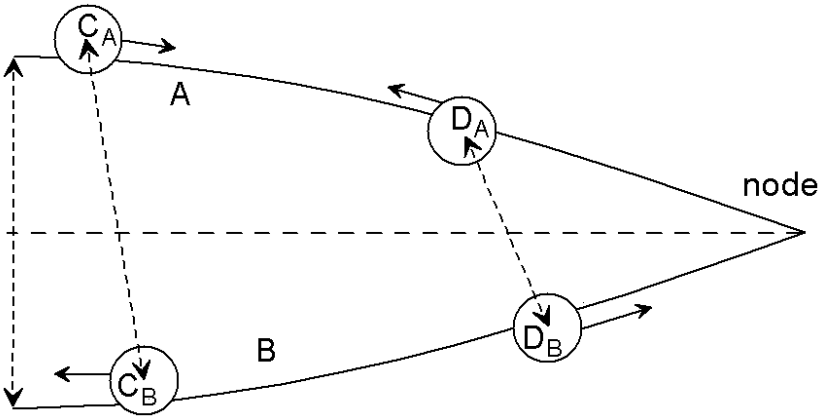

Fig. 2. Positions and net forces of hydrophobic (CA, CB) and hydrophilic (D_A, D_B) particles separated by a half-period of a standing wave.

the case for small enough particles. Both mechanisms produce a force difference proportional to the squared wave amplitude, making it a nonlinear effect. This conclusion is supported by analytical calculations in the next section [10].

2 Dynamics of a floating particle on a standing wave: The model

The model considers the particle drift as a function of four parameters: the wave length and amplitude, surface tension coefficient and particle mass. Consider a standing wave with a horizontal surface velocity $u(x,t) = u_0 \sin\omega_k t \cos kx$, vertical velocity $w(x,t) = u_0 \sin\omega_k t \sin kx$ and elevation $\zeta(x,t) = -(u_0/\omega_k)\cos\omega_k t \sin kx$, and with a small amplitude: $\epsilon = ku_0/\omega_k \ll 1$. We see that the points of the surface move by straight lines with the inclination $w/u = \tan kx$. For a particle of the mass M floating on a liquid with the density ρ and viscosity ν, the depth of the submerged part, δ, satisfies the vertical component of the equation of motion [11,12]

$$M\left(\frac{d^2\delta}{dt^2} + \gamma_v \frac{d\delta}{dt}\right) = F(\delta) = (g + \ddot{\zeta})[M - m_d(\delta)] + F_c(\delta)\,. \tag{1}$$

Here $m_d = \pi\rho(a\delta^2 - \delta^3/3)$ is the mass of the displaced fluid, and a is the particle radius presumed much smaller than the wavelength. The capillary force is given by the formula $F_c(\delta) = 2\pi r\alpha \sin(\phi + \theta)$. Here $r = \sqrt{2\delta - \delta^2/a}$ is the waterline radius, α is the coefficient of surface tension, ϕ is the angle between the ball surface and unperturbed water surface at the waterline and θ is the contact angle (see Figure 3). The formula looks particularly simple in the limit cases of extreme wetting ($\theta = 0$) or non-wetting ($\theta = \pi$): $F_c(\delta) = 2\pi(2\delta - \delta^2/a)\alpha$ taking α positive/negative for hydrophilic/hydrophobic particles. Capillary force is relevant for particles with $a < \sqrt{\alpha/\rho g}$ (smaller than a few millimeters for glass in the water). The coefficient of viscous friction can be estimated as $\gamma_v \sim 4\pi\rho\nu d/M$ where $d = r$ for $\delta < a$ and $d = a$ for $\delta > a$. We assume for simplicity that the depth oscillates weakly: $\delta(t) = \delta_0 + \delta_1(t)$ with $\delta_1 \ll \delta_0$. The zeroth approximation in the small parameter, δ_1/δ_0, gives the equation for the mean depth: $F(\delta_0) = 0$ where the stable solution with $F'(\delta_0) \equiv -M\Omega^2 < 0$ must be taken. For the oscillating part we get assuming $\Omega \gg \omega_k, \gamma_v$:

$$\delta_1(x,t) = \omega_k u_0 \Omega^{-2}[1 - m_d(\delta_0)/M] \sin kx(\cos\omega_k t + \gamma_v \omega_k \Omega^{-2} \sin\omega_k t)\,. \tag{2}$$

Horizontal projection of the equation of motion looks as follows:[1–3]

$$\frac{d}{dt}Mv = m_d\frac{du}{dt} + M\gamma_h(u - v) + \frac{d}{dt}[m_{ad}(u - v)] + F_c\zeta_x\,. \tag{3}$$

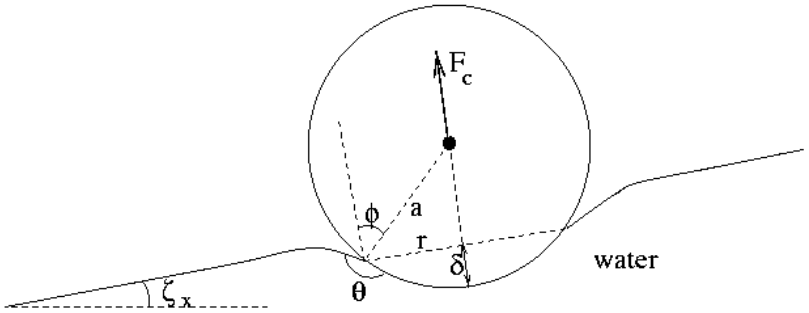

Fig. 3. Spherical particle on the inclined water surface. Notations and the direction of the capillary force F_c.

In the right hand side, the first term is the force that would act on the particle if it moves with the fluid (what Batchelor calls an effective "buoyancy" force[2]), the second term is due to the relative motion with m_{ad} and γ_h being respectively the added (virtual) mass and the horizontal friction rate, both generally dependent on $\delta(x,t)$. Note that $m_{ad} \propto m_d$. The last term in (3) appears because the capillary force is perpendicular to the water surface so that it has horizontal projection proportional to the inclination angle $\zeta_x \equiv d\zeta/dx$. We presumed the particle sliding rather than rolling which requires $\delta_0 > a\zeta_x^2/2$.

We rewrite the equation (3) in the following form

$$\left[M\gamma_h + \frac{d}{dt}(M + m_{ad})\right](v-u) = f(x,t) = \left[m_d(\delta) - M - \frac{F_c(\delta)k}{\omega^2}\right]\frac{du(x,t)}{dt}. \tag{4}$$

The general solution of the equation (4) needs expanding the rhs both with respect to δ and with respect to $x = x_0 + \int^t v(t')dt'$. Here we consider the simplest cases when in the first order $v \approx u$ and there is no need to expand with respect to x. First, this is so in the case of long gravity waves when $g\zeta_x = -du/dt$ and $\omega^2 = gk$. In this case, (4) takes the form

$$\left[M\gamma_h + \frac{d}{dt}(M + m_{ad})\right](v-u) = f(x,t) = \left(m_d - M - \frac{F_c}{g}\right)\frac{du}{dt} = (M-m_d)\frac{\ddot{\zeta}}{g}\frac{du}{dt}. \tag{5}$$

Here we substituted (1) assuming $\Omega \gg \omega_k \gg \gamma_v$. We see that the force $f(x,t)$, which causes the horizontal motion of the particle relative to the fluid, appears, as expected, in the second order with respect to the wave amplitude. We disregarded the nonlinearity of the wave itself which contributes the net drift of the particles only in the next order in ϵ. The net force (averaged over the wave period) is nonzero:

$$f(x) \equiv \int_0^{2\pi/\omega_k} f(x,t)\,dt = ku_0^2(M-m_d)\sin 2kx/2. \tag{6}$$

For the case of a strong horizontal friction, also in the first order $v \approx u$ so that the first-order term coming from expansion with respect to x gives zero net effect. The drift is determined by the net force which now takes the form

$$\overline{f(x,t)} = \frac{(M-m_d)}{\omega^2}\left[1 + \frac{m_d'(\omega^2-gk)}{M\Omega^2 k}\right]\overline{\ddot{\zeta}\,\dot{u}} = \frac{1}{2}ku_0^2(M-m_d)\left[1 + \frac{m_d'(\omega^2-gk)}{M\Omega^2 k}\right]\sin(2kx). \tag{7}$$

Generally, one also needs to account for the relative motion already in the first order. Consider the case of weak friction where the net force

$$f(x) = \frac{(M-m_d)(gk-\omega^2)}{\omega}(x-x_0)\overline{\frac{\partial}{\partial x}\frac{du(x,t)}{dt}} + \frac{(M-m_d)}{\omega^2}\left[1 + \frac{m_d'(\omega^2-gk)}{M\Omega^2 k}\right]\overline{\ddot{\zeta}\,\dot{u}}. \tag{8}$$

Here the particle displacement $x - x_0 = \int^t v(t')\,dt'$ and the velocity is taken in the first order

$$(M + m_{ad})v \approx \left[(M - m_d)\frac{gk}{\omega_k^2} + m_d + m_{ad}\right] u. \tag{9}$$

Note that generally $\omega_k^2 \geq gk$ so that the velocity of a light hydrophilic particle ($M < m_d$) exceeds fluid velocity while a heavy hydrophobic particle moves slower. Substituting (9) into (8) we get

$$f(x) = \frac{1}{2}ku_0^2\,(M - m_d)\sin 2kx \cdot \left[1 + \frac{m_d'(\omega^2 - gk)}{M\Omega^2 k} - \frac{\omega^2 - gk}{\omega^2}\left(1 - \frac{M - m_d}{M}\frac{\omega^2 - gk}{\omega^2}\right)\right]. \tag{10}$$

We see that in all cases the net force is a gradient of potential energy, $f(x) = -dU/dx$, where $U(x) \propto (M - m_d)\cos 2kx$. In a system with a friction, particles settle into the minima of the potential energy. The positions of the minima depend on the sign of $M - m_d$, which is negative/positive for hydrophilic/hydrophobic particles. We thus conclude that hydrophilic/hydrophobic particles must settle into the nodes/antinodes of the standing surface wave.

We conclude that the effect appears in the second order with respect to the wave amplitude. We disregarded the nonlinearity of the wave itself which contributes the net drift of the particles only in the next order in ϵ.

3 The experimental set up and procedures

A convenient way to generate a standing wave is to use a parametric Faraday instability [2]. A vertically oscillating fluid layer with a free surface becomes unstable when the oscillation amplitude A becomes greater than a critical value A_c. In a bounded cell a standing wave pattern is formed at a small super-criticality, $A - A_c$. A manifold of the arising wave patterns is well documented experimentally, see for example [13] for the wave pattern study in a low aspect ratio cell.

Our experimental set-up is similar to that used and described by Gollub and co-workers [14] and is shown schematically in Fig. 4. Standing waves are generated in a small rectangular cell (C) with horizontal dimension 58×9.6 mm and depth 10 mm. The cell walls are made from acrylic glass and the bottom and cover are from glass providing enhanced optical quality. Precision of horizontal alignment of the cell and its edges was up to $3'$. The cell is sealed to avoid surface contamination and evaporation of liquid. A thermo-stabilization to the level 0.2 °C was implemented in long run experiments. The vertical vibrations of the cell were provided by an electromagnetic shaker V (V20, Gearing and Watson Electronics Ltd) whose oscillation amplitude and frequency are controlled by a digital synthesizer (Wavetek 81). The shaker generates sinusoidal oscillations in the frequency range 5–400 Hz and with amplitudes up to 50 m/sec^2. The amplitude is measured by an MEMS accelerometer (ADXL150, Analog Device) attached to the moving frame. A 16-bit multifunction digital acquisition board NI-PCI-6035E with LabView software is used to digitize the signal from the accelerometer and calculate the amplitude of acceleration. All mechanical and optical parts of the set-up are mounted on a massive pneumo-isolated optical table.

The cell is filled with purified water (resistivity > 18 MΩ · cm). Water wets the acrylic walls. A meniscus appearing due to the boundaries on a static surface produces harmonic modes during oscillations [13]. In addition, a static surface inclination causes particle drift towards the walls or to the center of the cell depending on particle wetting. This drift may destroy the initial distribution of particles. To eliminate the meniscus effects we used pinned, brim-full, boundary conditions filling the cell precisely up to the level of the edge of lateral walls. The level of water was adjusted through a capillary tube at the bottom of the cell. The flatness of the static liquid surface was monitored optically, using a wide collimated laser beam from CW laser. These measures allow to adjust a level of water in the cell with the precision about 20 μm.

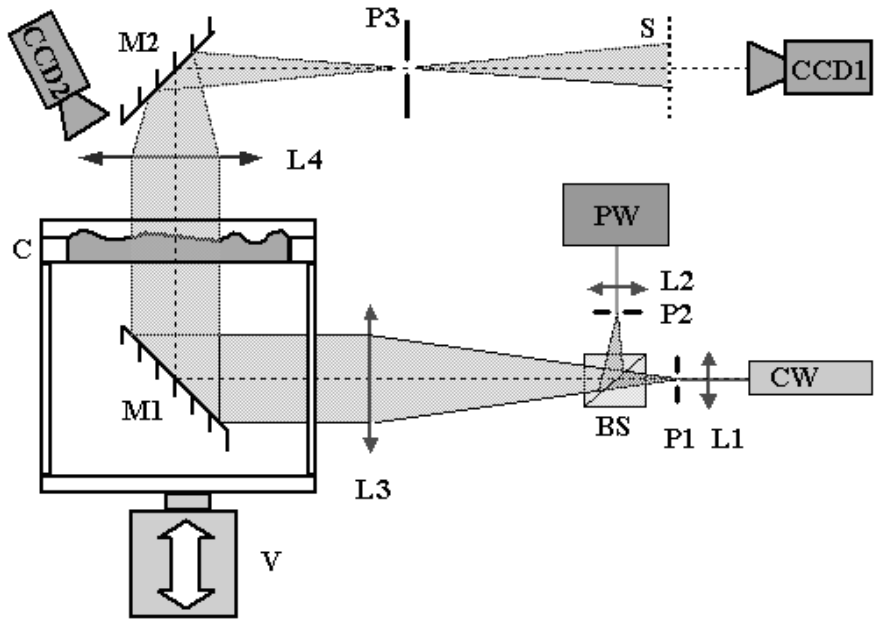

Fig. 4. Experimental set-up. The cell C filled with water is driven by an electromagnetic shaker V and is illuminated from below by a continuous (CW) or pulsed (PW) lasers. The lens L1, L2 and the pin-holes P1, P2 expand the laser beam to the diameter of 50 mm. The lens L3 with the pin-hole P3 in the focal plane of L3 form the image of surface wave anti-nodes on the screen S. The CCD2 is inclined to the main optical axis by the angle 10°. Pulsed Yag laser, PW, is used for recording the images with moving particles.

A droplet of suspension of particles is gently put on the surface of water just before sealing the cell and final water level adjustment. To observe the particle clustering on a standing wave we used hydrophilic particles with average diameter 30 μm and density 0.6 g/cm^3. The particles were sifted from the powder of glass bubbles (S60HS, 3M ScotchLite), separated by flotation in acetone (density 0.78 g/cm^3) and washed in pure water.

Illuminating optics was built on the shadowgraph principle and combines the light from the continuous 20 mW He-Ne laser CW and pulsed 120 mJ Yag laser PW. The cell was illuminated from bellow by an expanded collimated laser beam formed by the pin-hole P1 and lenses L1-L2. The continuous laser was used for the cell adjustment and visualization of wave patterns. The pulsed laser was used to record images of particle distribution. The parallel rays passing through the cell are refracted by waves and collected by the lens L3 of focal length 250 mm. A screen P2, positioned at focal plane of L3, has a 0.1 mm pin-hole centered at the system optical axis, such that the non-refracted light will pass through the pin-hole and form an image of antinodes on the screen S. The refracted light from CW laser illuminates an area in the focal plane P2. The size of this area on the image integrated with an exposure time greater than one period of the wave is proportional to the wave amplitude.

Two high-resolution (2048 × 2048 pixels) cameras CCD1 and CCD2 from Dantec PIV system were used to record the wave pattern and particle distribution simultaneously. The camera CCD1 collects images of anti-nodes. The camera CCD2 collects the light scattered by the particles on the surface. The camera CCD3 (not shown on the scheme) has resolution 720 × 480 and records images from the plane P2 used for wave amplitude measurements. The axes of CCD2 and CCD3 are inclined to the main optical axis at the angle 10 degrees. A calibration procedure was applied to compensate image distortions due to this inclination. CCD1 shutter is open for a time equal to the one period of the parametric wave. CCD2 camera is positioned off axis (and inclined) to avoid straight laser light and its shutter was opened for a shorter time ($\sim$ 1 ms) to prevent smearing of particles in the images. In addition the CCD2 shutter is synchronized in phase with the cell oscillations such that the shutter is opened when

the liquid surface is nearly flat. This allows to keep CCD2 at a minimal angle to the system's optical axis. The optical axis of CCD2 is perpendicular to the cell long axis.

4 Clustering of particles floating on a standing wave

We found it relatively easy to observe the drift of hydrophilic (wetted) particles in a stationary standing wave. An initially dispersed suspension of hollow glass spheres concentrates in the nodes of the surface wave during 2–100 seconds depending on the wave amplitude and frequency and remains there indefinitely long, Fig. 5.

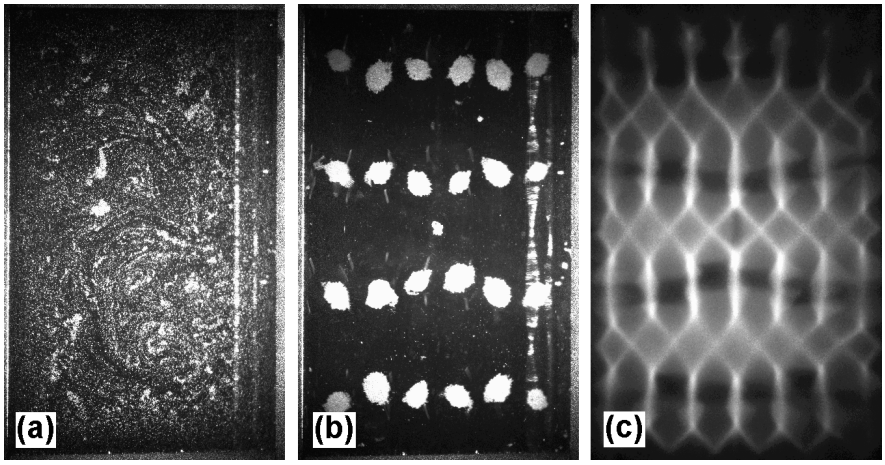

Fig. 5. Formation of particle clusters and wave pattern: a) initial particle distribution on a flat water surface, b) particle clusters in the nodes of the standing wave, c) anti-nodal pattern of the standing wave. The images in a) and b) were recorded by CCD2 and in c) by CCD1.

Since we found it impossible to mix particles without destroying the surface pattern, our procedure for measuring the clustering time for different amplitudes and frequencies was as follows. For each frequency and wave pattern we determined a threshold A_c for parametric instability and found an interval of oscillation amplitudes with a stationary surface wave pattern and particle clusters distribution on it. We observed that particles start to move a bit earlier, at less oscillation amplitudes, and before a non-stationarity in the wave pattern becomes visible. Each experimental run has been started from the mixing: the shaker amplitude was kept at $A \sim 5A_c$ for a couple minutes and then lowered to $A \sim 0.9A_c$. Next, a desired amplitude of vibration $A_i > A_c$ is set and the acquisition of images by both CCD1 and CCD2 is started. The unstable parametric wave appears after a time delay with an amplitude growing up to a stationary value proportional $(A_i - A_c)^2$. A set of collected images always starts from the moment when there are neither waves nor particle motion and ends when a new stationary state is reached with the developed wave and stationary particle clusters. After the parametric wave appears, the homogeneous area in CCD1 images is replaced by a network of lines corresponding to the wave anti-nodes, see Fig. 5(c). The width of the the lines decreases as the wave amplitude increases, and the maximum of intensity is constant across the line. So the variance of the light intensity averaged over an image area can be chosen as an indicator of moments when the waves appear and become stationary. The number of frames collected for each camera is 100 and the frame rate is adjusted using preliminary test runs.

A time interval between the moment when the wave appears (the variance of intensity from CCD1 images start to grow up) and stabilization of particle concentration variance (the variance of light intensity from CCD2 reaches a stationary value) is used as a characteristic time of clustering. The inverse clustering time is plotted versus the squared wave amplitude in Figure 6. The averaged wave amplitude $\langle A^2 \rangle$ has been estimated measuring a size of the spot

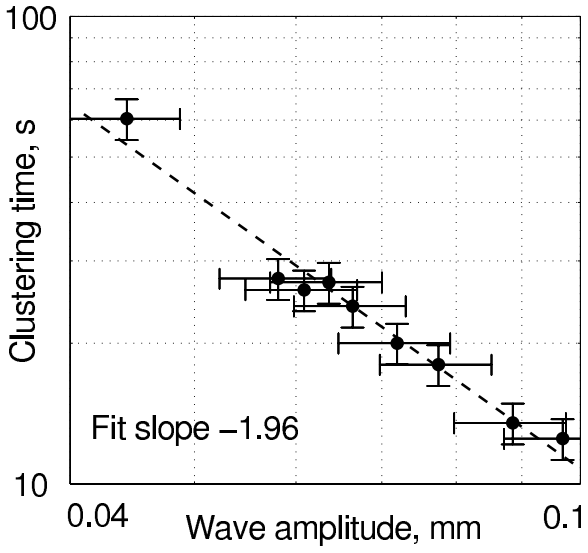

Fig. 6. Clustering rate *vs* wave amplitude. Quadratic dependence of inverse clustering time on A agrees with formula (10).

S_x, S_y in the focal plane P2 of the lens L3. The spot images were recorded by CCD3. For the refractive index of water 1.33 and small wave amplitudes, the angles S_y/F and S_x/F (where F is the focal length of L3) are equal to one third of the maximum surface inclination. It follows from Fig. 6 that within 10% the inverse clustering time is proportional to the square of the wave amplitude, as predicted by the model Eq. (10).

Specific characteristics of hydrophobic particles forced us to change experimental conditions. We did not have the hydrophobic hollow spheres to prepare the suspension and then used large heavy spheres, 1.6 mm PTFE balls with specific gravity 2.2, and observed their drift as an individual particle. The oscillation and drift of such a sphere is shown on Fig. 7 made by stroboscopic method. The stroboscope frequency was twice the frequency of the surface wave (12.6 Hz) and the phase of flashes was adjusted to see the maximal and minimal surface positions. The ball can be moved without noticeable wave distortion using a thin metal needle touching the liquid surface near the ball. A meniscus formed by the needle generates a repulsive force that can be used to move the ball. Initially a PTFE ball was position near the wave node. After release the ball moves towards the anti-node, from the left to the right in Fig. 7. The time interval to reach the anti-node depends on wave amplitude and ranges from 2 to 20 seconds.

5 Statistics of floater distribution in chaotic waves

Quasi-linear standing waves exist only when shaker vibration amplitudes are small enough. At higher amplitudes, the standing wave loses stability and chaotic spatio-temporal regimes arise [13,14]. Chaotic waves generate random compressible flow on the liquid surface, which is expected to produce a very inhomogeneous particle distribution [15–19]. Clustering in a smooth random flow is expected to result in a multi-fractal distribution [18]. In addition, inertia of the floaters may lead to the crossing of different particle paths and creation of caustics [22,23].

Consider a number of particles inside a circle of radius r around the point $\mathbf{x}$: $n_r(\mathbf{x})$. How do the statistics of the random field $n_r(\mathbf{x})$ change with the scale of resolution r? Such a change can be characterized by the scaling exponents, ζ_m, of the moments: $\langle n_r^m \rangle \propto r^{\zeta_m}$. Note that $\zeta_0 = 0$ and $\zeta_1 = 2$. When the distribution is smooth on a surface, one expects $\zeta_m = 2m$. When this equality breaks for some m, one usually calls the distribution fractal. A recent theory for a short-correlated compressible flow [15,18] gives the set of the exponents ζ_m depending nonlinearly on m, which corresponds to a multi-fractal distribution (those theoretical formulas give the Lagrangian exponents which in our notations are $\zeta_{n+1} - 2$). Multifractality of the measure means that the statistics are not scale-invariant: strong fluctuations of particle concentration

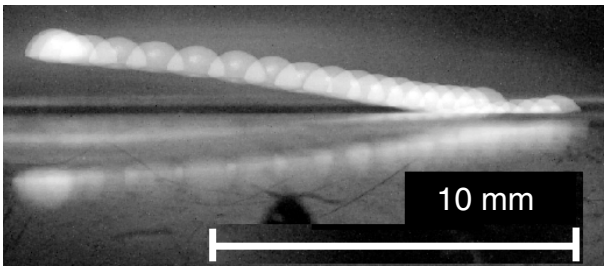

Fig. 7. Hydrophobic teflon ball of 1.6 mm diameter placed gently on a water surface moves towards the antinode, from the right to the left, on the standing wave.

are getting more probable as one goes to smaller scales (increasing resolution). The fractal (information) dimension for a random surface flow has been measured by Sommerer and Ott, who found non-integer $d = d\zeta_m/dm|_{m=0}$ [19]. Additionally, the scaling of the second moment has been found and related to the correlation dimension (again non-integer) [20, 21]. Therefore, fractality of the distribution has been established in [19–21]. To the best of our knowledge, different dimensions have not been compared for the same flow (when found different, that demonstrates multifractality as in our measurements presented below).

In the second part of the experiment we measured the moments of the concentration per unit area (defined as $n_r r^{-2}$) for the suspension of small hydrophilic particles mixed by a random flow of surface waves (at the driving amplitude $\sim 2A_c$). Note that at such an amplitude, it is not yet developed turbulence but rather few interacting modes that provide for a Lagrangian chaos. The experiment has been done for the set of the oscillation frequencies from 30 to 220 Hz and the amplitudes $1.8 - 2.5A_c$. We reproduce here a typical result for the parametric wave with

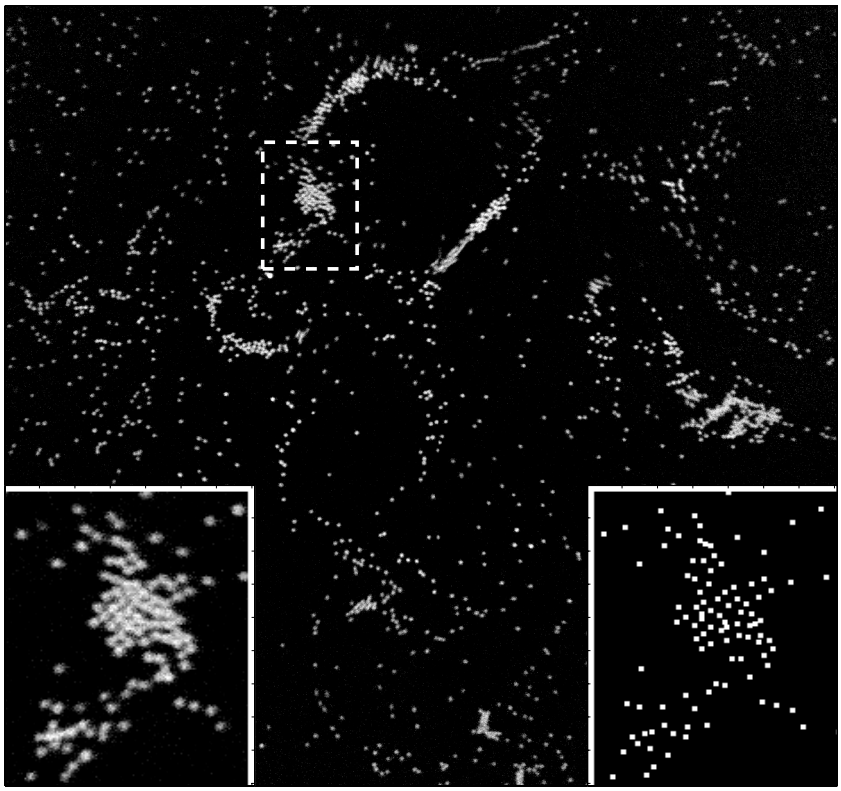

Fig. 8. A snapshot of particle distribution in random waves. The number of particles is 920. The wave frequency is 32 Hz. The image size is 17×17 mm. The left inset shows a zoomed-in image of the marked particle cluster. The right inset shows the result of particle recognition procedure.

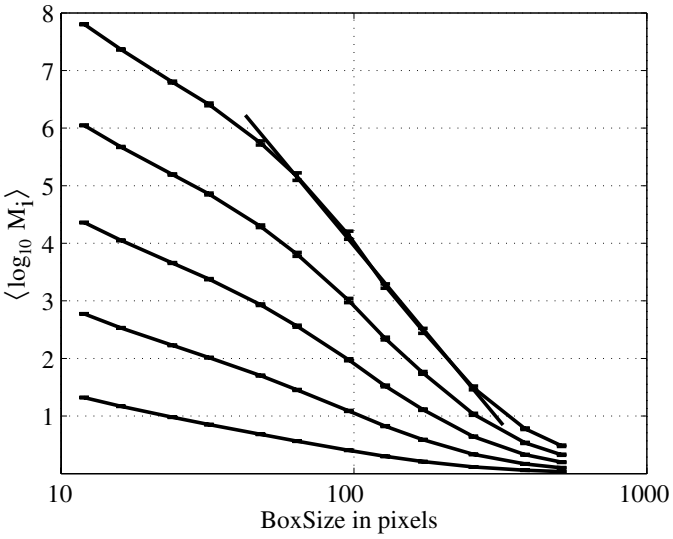

Fig. 9. Averaged moments of particle concentration, from 2^{nd} to 6^{th}, versus the scale of coarse-graining.

the frequency 32 Hz, the wavelength about 7 mm at the oscillation amplitude 198 μm $\simeq 2A_c$. A snapshot of the floater distribution for this set is shown in Figure 8.

The most reliable approach to quantify the particle concentration is to recognize and count individual particles. We used 95 μm fluorescent microspheres with the density 1.05 g/cm^3 floating in 20% salt (NaCl) solution in water. Fluorescence greatly improves the image contrast, eliminates spurious refractions, and allows positioning the CCD2 camera with an optical filter on the system optical axis. In this experiment, we used a continuous wave 6 W argon ion laser (CW laser on Fig. 4) for illumination and the bigger cell 50×50×10 mm with a greater number of waves. The illumination scheme was the same as in the experiments with standing waves excluding the pulsed laser (PW) laser. The size of the observation area is 30×30 mm, the pixel size 15 μm and the mean particle diameter corresponds to 6-7 pixels. Prior to particle recognition the images were preprocessed. The background noise was subtracted using a threshold equal to the mean intensity plus 3 standard deviations. The resulting images were smoothed by convolution with a gaussian shape 5×5 pixels mask (two dimensional low pass filter). The particle coordinates were determined maximizing the correlation of the image with the 3×3 gauss-shape matrix. The method was validated by comparing the number of particles with that estimated during the emulsion preparation. The particle detection in the dense clusters was verified by direct visual inspection of images. No particle overlaps were observed, see insets in Fig. 8. The error in the particle coordinate is less then ±1 pixel or ±15μm.

Over 1000 images with particle distributions were recorded with the sampling time interval 4 sec. A typical standard deviation of the number of particles in the open area 30 × 30 mm averaged over 1000 images is less than 10. The first six moments of the coarse-grained concentration, $N_m = \langle n_r^m \rangle r^{-2m} \propto r^{\zeta_m - 2m}$, are shown in Figure 9 versus the scale of averaging (bin size r). The bars show the standard errors in determining the moment. We see that indeed the moments with $m > 1$ grow when r decreases below the wavelength of the parametrically excited mode. This growth slows down when r decreases below $r = 50$ pixels [$\log_{10}(50) \simeq 1.7$]. This is possibly due to the dense clusters where the finite particle size, short range repulsion, and the particle back reaction on the flow are important. An additional reason may be an insufficient representation of dense regions by the finite number of particles. We found that in the interval $50 < r < 300$ pixels the data can be approximated by the straight lines which correspond to the power laws on this log-log plot. The scaling exponents are shown in Fig. 10. The nonlinearity of the dependence of ζ on m can be interpreted as the first experimental sign of multifractality in the distribution of particles.

Another interesting aspect of the floater motion is related to inertia which may cause particle paths to intersect. This phenomenon was predicted in [22] and was called the sling effect, it must

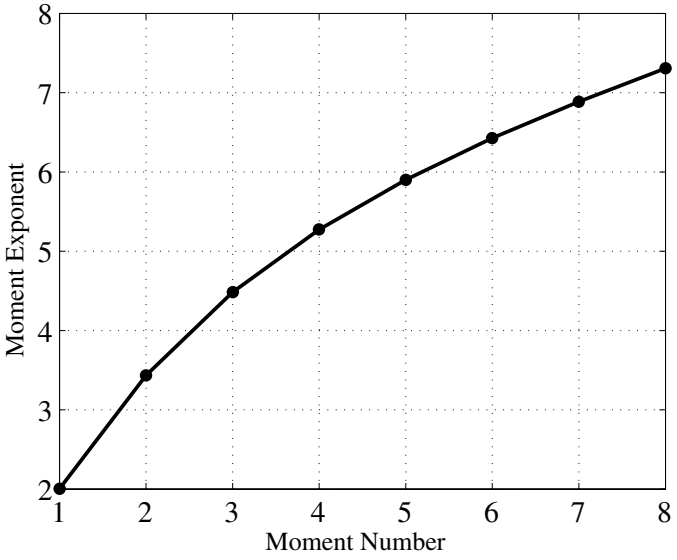

Fig. 10. Scaling exponents of the moments of particle number versus the moment order.

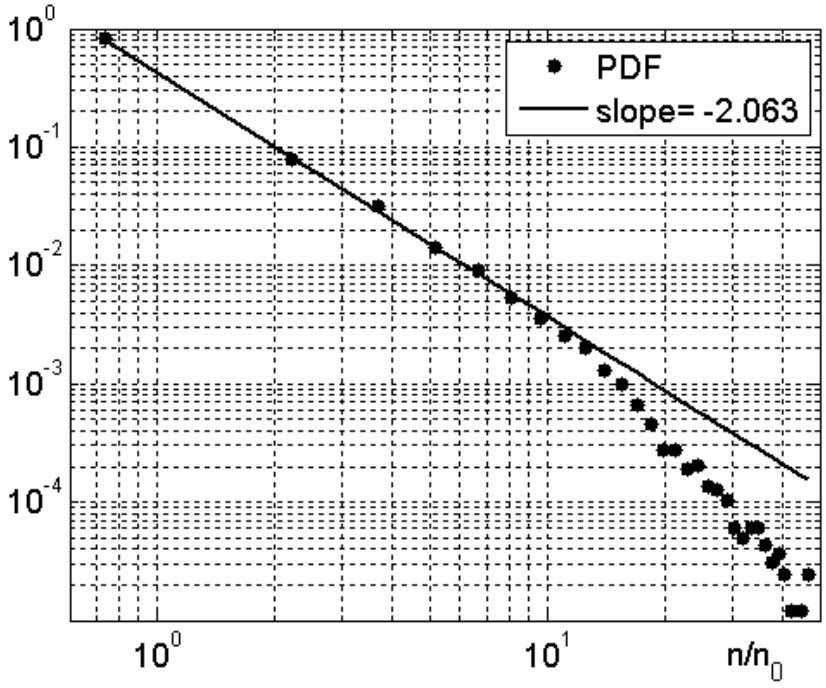

Fig. 11. The probability density function of particle concentration in the box 64 x 64 pixels (0.96 × 0.96 mm). The average number of particles in the box $n_0 = 2.1$. The straight line is $P \propto n^{-2}$ presumably due to caustics.

lead to the appearance of caustics in the particle distribution [23]. At weak inertia (like in our system), caustics are (exponentially) rare [22,23] yet we are likely to see them at the center of Fig. 9. Indeed, as argued in [22], breakdowns of particle flow are mostly one-dimensional so that caustics must look locally like two parallel straight lines. One-dimensional folds in the particle distribution lead to an explosive growth of the concentration, $n \propto (t_0 - t)^{-1}$ [22], which produces a power-law tail in the concentration probability density function (PDF): $P(n)dn \propto dt \propto dn/n^2$. Indeed, in the inset in Fig. 11 we show the PDF of particle numbers obtained from $2 \cdot 10^5$ bins of the size 64×64 pixels. The straight line corresponds to n^{-2}. A single-point PDF does not contain the whole information on the statistics so that our result does not rigorously prove the existence of caustics. Yet it gives strong support to the predictions of [22, 23] that caustics must

appear in a system of inertial particles. At higher inertia, multiple crossings of particle paths provide for extra mixing that makes the sum of Lyapunov exponents positive and the measure smooth (rather than multi-fractal) [24,25].

6 Conclusion

The main idea of this work is that the surface tension makes a small floater inertial. Depending on the sign of capillarity, the mass inertia may be either positive or negative for hydrophobic or hydrophilic floating objects correspondingly. This inertial effect influences particle dynamics and leads to the particle drift and clustering on the surface waves. We presented the dynamical model describing particle drift in the standing wave. The model predicts that the particle drift velocity is proportional to the square of the wave amplitude. It is confirmed by experimental observations of particle dynamics on the surface waves generated by Faraday instability. The experiments show that hydrophilic particles cluster in the nodes and hydrophobic in the antinodes of the standing surface wave. The clustering time was measured for small hydrophilic hollow glass spheres at different wave amplitudes. It has been shown that the rate of clustering is proportional to the square of the wave amplitude that agrees with the model prediction.

The experiments with particle dispersion by chaotic surface waves demonstrate that particles form clusters with a short life time on the scales less then the wavelength. The moments of concentration of particles show scaling behavior at the scales intermediate between the wave length and the distance between the particles. The dependence of the moment exponents of the moment order shows deviation from a straight line which is an indication that particles concentrate on a multi-fractal set. Statistical signatures of co-existence of caustics and multi-fractals needs further studies.

References

1. J.S.W. Rayleigh, Proc. Roy. Soc. **1**, 1 (1884)
2. M. Faraday, Phil. Trans. R. Soc. Lond. **121**, 299 (1831)
3. L.V. King, Proc. Roy. Soc. London A **147**, 212 (1934)
4. G. Whithworth, M.A. Grundy, W.T. Coakley, Ultrasonics **29**, 439 (1991)
5. G. Falkovich, A. Weinberg, P. Denissenko, S. Lukaschuk, Nature **435**, 1045 (2005)
6. J. Lighthill, Waves in Fluid. (Cambridge University Press, 1978)
7. P.A. Krachevsky, K. Nagayama, Adv. Coll. Sci. **85**, (2000) 145
8. M.M. Nicolson, Proc. Camb. Philos. Soc. **45**, 288 (1949)
9. D. Vella, L. Mahadevan, Am. J. Phys. **73**, 814 (2005)
10. G. Falkovich, A. Weinberg, P. Denissenko, S. Lukaschuk, Nature www.nature.com/nature/journal/v435/n7045/suppinfo/4351045a.html
11. L. Landau, E. Lifshits, Fluid Mechanics (Pergamon Press, Oxford, 1987)
12. M.R. Maxey, J.J. Riley, Phys. Fluids **26**, 883 (1983)
13. S. Douady, J. Fluid Mech. **221**, 383 (1990)
14. B.J. Gluckman, C.B. Arnold, J.P. Gollub, Phys. Rev. E **51**, 1128 (1995)
15. E. Balkovsky, G. Falkovich, A. Fuxon, Phys. Rev. Lett. **86**, 2790 (2001)
16. G. Falkovich, K. Gawedzki, M. Vergassola, Rev. Mod. Phys. **73**, 913 (2001)
17. A. Balk, G. Falkovich, M. Stepanov, Phys. Rev. Lett. **92**, 244504 (2004)
18. J. Bec, K. Gavedzki, P. Horvai, Phys. Rev. Lett. **92**, 224501 (2004)
19. J.C. Sommerer, E. Ott, Science **259**, 335 (1993)
20. J.C. Sommerer, Phys. Fluids **8**, 2441 (1996)
21. A. Nameson, T. Antonsen, E. Ott, Phys. Fluids **8**, 2426 (1996)
22. G. Falkovich, A. Fouxon, M. Stepanov, Nature **419**, 151 (2002)
23. M. Wilkinson, B. Mehlig, Europhys. Lett. **71**, 186 (2005)
24. J. Bec, J. Fluid Mech. **528**, 255 (2005)
25. B. Mehlig, M. Wilkinson, Phys. Rev. Lett. **92**, 250602 (2004)